Environmental Science: Atmospheres

ROYAL SOCIETY OF CHEMISTRY

PAPER

View Article Online
View Journal | View Issue

Cite this: *Environ. Sci.: Atmos.*, 2024, **4**, 767

Quantifying the drivers and heterogeneity of global total precipitable water†

S. Maishal *

Total precipitable water (TPW) is a key player in the global water cycle, shaping our climate and impacting extreme weather phenomena such as tropical storms and monsoons. Its presence, varying across regions and seasons, is the highest in warm oceanic regions, particularly in the tropics and subtropics, while polar regions see the least. Multiple satellite observations provide compelling evidence of a positive and statistically significant trend in TPW, indicating a notable increase at a rate of 0.037 kg per m^{-3} per year. Ocean temperatures vary regionally; the North Atlantic Ocean (NAO) warms at 0.02–0.03 °C per year and South Atlantic Ocean (SAO) warms slower at 0.015–0.020 °C per year. The Equatorial and Northeastern Pacific warm at 0.038–0.040 °C per year. The Indian Ocean (IO) warms the fastest at 0.1–0.18 °C per year, and Southern Ocean (SO) and Atlantic Ocean (AO) show mixed trends, including cooling. The intricate relationship between natural climate indices and the global TPW received strong positive feedback from the Pacific decadal oscillation (PDO) and oceanic Niño index (ONI), indicating their profound impact on TPW. The Western Pacific index (WP) exhibits a direct and strong positive feedback loop and a strong relationship of PDO and ONI with TPW. Increasing the α level enhances connections, notably between the multivariate ENSO index (MEI) and dipole mode index (DMI). Interactions between these indices and TPW unveil interconnected climatic processes affecting atmospheric moisture. Recognizing these dynamics is crucial for accurate climate predictions, given the reinforcement of positive feedback loops.

Received 11th March 2024
Accepted 18th May 2024

DOI: 10.1039/d4ea00030g

rsc.li/esatmospheres

Environmental significance

TPW plays a crucial role in the global water cycle, significantly impacting climate dynamics worldwide. It goes beyond mere presence, actively influencing the development of extreme weather events such as tropical storms and monsoons. TPW distribution varies across regions, with higher concentrations typically observed in warm oceanic areas, especially in tropical and subtropical climates, while polar regions exhibit lower levels. Satellite observations reveal a noticeable upward trend in TPW, indicative of its increasing importance. Meanwhile, ocean temperatures exhibit diverse trends across different regions. For example, the North Atlantic Ocean (NAO) experiences a positive shift, the South Atlantic Ocean (SAO) shows a more modest warming trend, and various warming trends are observed in the Equatorial Pacific, Northeastern Pacific, and Indian Ocean. The interaction between natural climate indices and TPW dynamics is complex, with strong positive feedback from phenomena like the PDO and ONI. The WP establishes a direct and robust positive feedback loop, highlighting the intricate relationship between PDO, ONI, and TPW. Additionally, as the α level increases, connections strengthen, revealing notable links from indices like the MEI and DMI. Understanding these interactions is crucial for accurate climate predictions. Observations of climate indices and TPW relationships across various oceanic regions unveil the complex processes shaping atmospheric moisture content. Positive feedback loops underscore the importance of deciphering these interactions to enhance the precision of climate forecasts and deepen our understanding of the global climate system. In essence, comprehending the interplay between natural climate indices and TPW is essential for advancing climate science and improving our ability to predict future climate trends.

1. Introduction

TPW is a critical parameter for understanding the global water cycle and its impact on the climate system.[1] The increase in TPW over the ocean due to the warming of the Earth's atmosphere is linked to more frequent and intense extreme weather events, such as floods and droughts.[2,3] TPW plays a crucial role in forming and intensifying tropical storms and hurricanes over the ocean.[4,5] The warm ocean waters provide the energy required to power these storms, and TPW determines the amount of moisture available for precipitation, fueling the storm's intensity.[6] The high levels of TPW over the ocean can lead to the formation of deep convection, resulting in thunderstorms and heavy rainfall, which can trigger flash floods and landslides.[7,8]

Conversely, low levels of TPW over the ocean can lead to droughts and dry spells, affecting the marine ecosystem and fisheries.[9] The distribution of TPW over the ocean influences

Centre for Ocean, River, Atmosphere and Land Sciences (CORAL), Indian Institute of Technology Kharagpur, Kharagpur 721302, India. E-mail: subhadeepmaishal@kgpian.iitkgp.ac.in; Tel: +91 8597577174

† Electronic supplementary information (ESI) available. See DOI: https://doi.org/10.1039/d4ea00030g

weather patterns and the occurrence of extreme weather events. Therefore, understanding the drivers of TPW and variability is crucial for effective climate modeling and weather forecasting.[9] Total precipitable water (TPW) distribution is highly heterogeneous spatially and temporally. Generally, TPW is the highest over the tropics and decreases towards the poles.[10] This is because warm, humid air is more prevalent in the tropics, while cold, dry air is more common at high latitudes. Over oceans, TPW tends to be higher in regions of warm sea surface temperatures, where evaporation is more significant. TPW can also vary seasonally, with higher values typically observed during the summer in the Northern Hemisphere and winter in the Southern Hemisphere.[11,12]

Climate change significantly affects TPW over the ocean, resulting in more intense and frequent extreme weather events. Warmer ocean temperatures caused by climate change provide the necessary energy to fuel these storms. At the same time, higher TPW levels increase the amount of moisture available for precipitation, leading to more intense and frequent storms. TPW is crucial in forming and intensifying hurricanes in the Atlantic Ocean and typhoons in the Pacific Ocean.[13,14] TPW also plays a vital role in the formation and intensity of monsoons in the Indian Ocean region. High TPW levels are often associated with monsoon seasons and changes in large-scale circulation, leading to heavy rainfall and flooding, as seen in the Indian state of Kerala in 2018.[15] Changes in ocean temperatures and atmospheric circulation patterns are the main drivers of TPW levels and their impact on extreme weather events.[15] These factors are interdependent and contribute to the complex and evolving nature of the Earth's climate system. Understanding the drivers of TPW and their connection to extreme weather events is crucial for predicting and mitigating the risks associated with climate change. Multiple interconnected factors, including temperature, atmospheric circulation patterns, and the availability of moisture sources, drive TPW levels. The atmosphere can hold more moisture as temperatures increase, leading to higher TPW levels. This effect is due to the warmer air's capacity to hold more water vapor than cooler air.[16] Atmospheric circulation patterns can affect TPW levels by altering moisture transport across regions.[17,18] These circulation patterns are influenced by factors such as ocean temperatures and land–sea temperature gradients, which can control the position and intensity of weather systems.[19,20]

Additionally, warmer sea surface temperatures can increase evaporation, increasing TPW levels in the surrounding atmosphere.[21,22] Finally, the availability of moisture sources such as precipitation, evaporation, and snow and ice melting can also affect TPW levels.[23] Understanding the interconnected drivers of TPW is crucial for predicting and mitigating the impacts of extreme weather events caused by changes in TPW levels. In addition, mesoscale circulation also affects the TPW in forming convective systems, such as thunderstorms.[24,25] These systems are often associated with mesoscale circulations, which transport moisture and heat, creating a favorable environment for developing clouds and precipitation. In a convective system, warm, moist air rises and cools, forming clouds and precipitation. As the air cools, its ability to hold water vapor decreases, releasing some water vapor as liquid or ice precipitation. This process can increase the amount of TPW in the atmosphere, particularly in regions with frequent convective systems, such as tropical and subtropical regions.

The latest IPCC report (AR6) projected that the TPW over the ocean would increase in all future emission scenarios. Specifically, the report notes that TPW over the ocean will likely increase global warming by 1–3% per degree Celsius.[26,27] This is more pronounced in the tropics compared to higher latitudes. This increase in TPW is attributed to warmer air holding more moisture. As the planet warms due to greenhouse gas emissions, there will be an overall increase in atmospheric moisture content. This increased moisture content can lead to more frequent and intense precipitation events, which can have significant implications for weather patterns, freshwater resources, and food and water security. TPW is a critical factor influencing global food and water security by controlling the availability and distribution of freshwater resources essential for agriculture and human consumption. Anthropogenic climate change has resulted in changes in TPW, leading to more frequent and intense precipitation events that negatively affect crop yields and food security. Additionally, changes in TPW affect freshwater resources, potentially leading to water contamination and reduced access to safe and clean water. These changes have significant implications for human health and well-being, highlighting the need for urgent action to address the underlying causes of climate change and implement measures such as water conservation, sustainable agriculture practices, and investment in water infrastructure. Failure to act may lead to severe consequences for global food and water security and the overall sustainability of our future.

Investigating the interconnections between diverse climate indices and TPW engenders valuable insight into the intricate associations prevailing amidst broad-scale climate patterns and atmospheric moisture content. TPW, as an integrative gauge of water vapor encompassing the vertical expanse of the atmosphere, represents a pivotal parameter enabling comprehension of precipitation patterns and atmospheric dynamics. Assorted climate indices are routinely employed as proxies for distinct climatic phenomena. Notably, the El Niño-Southern oscillation (ENSO) index captures the variances in sea surface temperatures and atmospheric circulation patterns within the tropical Pacific. Positive ENSO phases (El Niño) typically engender augmented TPW attributable to intensified evaporation over warm oceanic surfaces, while negative ENSO phases (La Niña) commonly correspond to diminished TPW. Moreover, indices such as the Pacific decadal oscillation (PDO) and the Arctic oscillation (AO) exhibit discernible associations with TPW. The PDO elucidates long-term fluctuations in Pacific Ocean sea surface temperatures, influencing atmospheric pressure systems and moisture transport. Positive PDO phases concomitantly correlate with heightened TPW in select regions, whereas negative phases exhibit an inverse relationship. The AO, characterizing the state of atmospheric circulation across the Northern Hemisphere, manifests influence on TPW through its impact on moisture transport and precipitation patterns. Positive AO phases are frequently linked to amplified TPW,

primarily within mid-latitudes, while negative phases result in reduced TPW.

Furthermore, indices such as the Indian Ocean dipole (IOD) and the North Atlantic oscillation (NAO) have demonstrated empirical connections with TPW. The IOD, typified by temperature gradients between the western and eastern Indian Ocean, exerts influence on atmospheric moisture convergence and divergence, thereby associating positive IOD events with heightened TPW over the eastern Indian Ocean and adjacent regions. The NAO, reflecting fluctuations in atmospheric pressure patterns over the North Atlantic, influences moisture transport and precipitation, with positive NAO phases also affecting the TPW in the region.

By articulating precise research inquiries, including examining the impacts of climatic variables on TPW distribution, comprehending the ramifications of climate change on TPW and extreme weather occurrences, and investigating empirical correlations with climate indices, this study endeavors to propel understanding within the field. This methodical approach facilitates a comprehensive exploration of the intricate interplay among TPW dynamics, climatic fluctuations, and extreme weather patterns. Ultimately, this endeavor aims to bolster climate modeling accuracy, enhance weather forecasting capabilities, and inform more effective decision-making concerning climate adaptation and mitigation measures.

2. Materials and methods

This study employed a 1° × 1° spatial resolution remote sensing system (RSS) version-7 gridded dataset of TPW. This dataset was meticulously generated by leveraging measurements from a myriad of sophisticated microwave radiometers in 1987–2022, including SSM/I, SSMIS, AMSR-E, WindSat, and AMSR2 satellite data.[28,29] The datasets were meticulously processed using a radiative transfer model (RTM) and precise instrument inter-calibration, ensuring that the resulting TPW product was of the highest quality and reliability.[30,31] The TPW-RSS product, derived from precise water vapor measurements, is particularly well suited for climate studies, providing unprecedented insights into the intricate dynamics of the global water cycle and the mechanisms underlying the formation and intensification of extreme weather events. The TPW retrievals random errors ranging from 0.2 to 0.4 kg m^{-2} due to radiometer noise.[32] In addition, it's also in very good agreement with *in situ* measurements made by ground-based global navigation satellite system (GNSS) retrievals of TPW.[33] The study employed the highly reliable 0.25° daily optimum interpolation sea surface temperature (OISST), version 2.1 data provided by NOAA/NCEI and this dataset is in very good agreement with ARGO *in situ* as well satellite measurement.[34] The global average root-mean-square difference (RMSD) for sea surface temperature stands at an exceptional 0.24 °C. For the assessment of near-surface air temperature and wind speed, NASA Global Modeling and Assimilation Office (GEMO) MERRA-2 datasets (MERRA2_100.instM_3d_ana_Np, v5.12.4) with a spatial resolution of 0.500° × 0.625° were used.[35] Different climate indices are acquired from the esteemed NOAA Physical Sciences Laboratory (PSL) for causal discovery analysis. These meticulous data sources and analytical approaches were chosen to ensure the utmost accuracy and reliability in this scientific investigation. The computation of climatology used the time average of the entire study period; a simple linear regression model was employed to estimate the trend. The study employed the PCMCI+ (partial correlation and multiple conditional independence) algorithm in the the period of 1987–2022, known for its efficacy in identifying causal drivers by conducting iterative conditional independence tests and calculating partial correlations between time series data.[36] The algorithm consists of two stages: the first stage uses a modified Peter-Clark (PC) algorithm based on the skeleton of the causal network. Given $\bar{X}_t = X_t^1, X_t^2, \ldots, X_t^N$, the set of all variables, to test for causality between all variable pairs from up to a maximum lag $\tau_{\max}$, one needs to test for causality using a maximum conditioning set of dimensions $N\tau_{\max}$. This stage reduces the dimensionality of the conditioning set by filtering out variables that have no significant contribution to the conditioning set. For each variable $\bar{X}_t^j \in \bar{X}_t$, after initializing preliminary parents $\overline{\mathcal{P}}(X_t^j) = (\overline{X}_{t-1}, \overline{X}_{t-2}, \ldots, \overline{X}_{t-\tau_{\max}})$ the following hypothesis is tested for all variable $\bar{X}_{t-\tau}{}^i$ from $\overline{\mathcal{P}}(X_t^j)$:

$$\mathrm{PC}: X_{t-\tau}{}^i \coprod X_t^j | S$$

For any set S with cardinality p, where S contains a subset of $\overline{\mathcal{P}}(X_t{}^j) \backslash \{X_{t-\tau}{}^i\}$, continuously increasing pp allows us to test the null hypothesis; if not rejected, the link is removed from P. Hence, the first iteration ($p = 0$) removes uncorrelated variables from $\overline{\mathcal{P}}(X_t^j)$. In the second iteration ($p = 1$), variables that become independent after conditioning on the highest correlated variable from the first iteration are removed from $\overline{\mathcal{P}}(X_t^j)$. In the third iteration ($p = 2$), these variables are removed from $\overline{\mathcal{P}}(X_t^j)$, which become independent after conditioning on the two strongest drivers from the previous iteration and so on. A lenient alpha level, as an example $\alpha = 0.1$ is taken for hypothesis testing in this stage so that true links are not lost. Thus, for each variable X_t^j, a reduced conditioning set is generated called 'Parents, $\overline{\mathcal{P}}(X_t^j)$', which contains all significant conditioning variables and some false positives depending on the choice of statistical significance. The second stage determines the parents of each driver variable through momentary conditional independence (MCI) tests, evaluating the statistical significance of causal links. To find the causal connections for every pair $X_{t-\tau}{}^i \rightarrow X_t^j$ conditioning on parents of X_t^j and $X_{t-\tau}{}^i$ is carried put in various time delays $\tau = \{1,2,\ldots,\tau_{\max}\}$, and the following null hypothesis is tested at $\alpha = 0.01$, 0.1, and 0.5.

$$\mathrm{MCI}: X_{t-\tau}{}^i \coprod X_t^j | \overline{\mathcal{P}}(X_t^j) \backslash \{X_{t-\tau}{}^i\}, \overline{\mathcal{P}}(X_{t-\tau}{}^i) \; \forall \, X_{t-\tau}{}^i \in X_t^-$$

where $X_t^- = (X_{t-1}, X_{t-1}, \ldots, X_{t-\tau_{\max}})$, $\overline{\mathcal{P}}(X_{t-\tau}{}^i)$, and $\overline{\mathcal{P}}(X_t^j)$ are the conditioning sets generated in the PC stage. Both stages (PC and MCI) use conditional independence tests to measure connection strength and statistical significance. PCMCI can use a linear and nonlinear test statistic based on partial correlation (ParCorr) and conditional mutual information using the k-nearest neighbor approach (CMI-knn). CMI for continuous

and possibly multivariate random variables X, Y, and Z is defined as

$$I_{X;Y|Z} = \int\int\int \mathrm{d}x\mathrm{d}y\mathrm{d}z p(x,y,z)\log\frac{p(x,y|z)}{p(x|z)\cdot p(y|z)} = H_{XZ} + H_{YZ} - H_Z - H_{XYZ},$$

where H denotes the Shannon entropy and where we assume that the densities $p(\cdot)$ exist. The task is to test the conditional independence hypothesis *versus* the general alternative:

$$H_0 : X \coprod Y|Z$$
$$H_1 : X \not\coprod Y|Z$$

From the definition of CMI it is immediately clear that $I_{X;Y|Z} = 0$ if and only if $X \coprod Y|Z$, provided that the densities are well-defined. Shannon-type conditional mutual information is theoretically well founded and its value is well interpretable as the shared information between X and Y not contained in Z. And the nearest-neighbor CMI estimator is based on

$$\hat{I}_{XY|Z} = \psi(k) + \frac{1}{n}\sum_{i=1}^{n}[\psi(k_i{}^z) - \psi(k_i{}^{xz}) - \psi(k_i{}^{yz})]$$

with the Digamma function as the logarithmic derivative of the Gamma function $\psi(x) = \frac{\mathrm{d}}{\mathrm{d}x}\ln\Gamma(x)$ and sample length n[1]. The only free parameter k is the number of nearest neighbors in the joint space of $\mathcal{X}\otimes\mathcal{Y}\otimes\mathcal{Z}$ which defines the local length scale ε_i around each sample point i. Then $k_i{}^{xz}$, $k_i{}^{yz}$, and $k_i{}^z$ are computed by counting the number of points with a distance strictly smaller than ε_i in the subspace $\mathcal{X}\otimes\mathcal{Z}$ to get $k_i{}^{xz}$, in the subspace $\mathcal{Y}\otimes\mathcal{Z}$ to get $k_i{}^{yz}$, and in the subspace $\mathcal{Z}$ to get $k_i{}^z$. Each link's significance is calculated at a 95% confidence level. This analysis utilized the innovative method PCMCI+, which extends PCMCI to incorporate the identification of contemporary links. To unravel potential drivers of TPW, this study employs a causal model within the Pearl causality (PC) framework, surpassing simple correlation analysis limitations. The complex and nonlinear relationship between TPW and natural climate processes (*e.g.*, ENSO, DMI, and PDO) is explored. The PCMCI algorithm, although limited by computational complexity, linearity assumptions, sensitivity to conditioning parameters, and challenges in interpreting results within the Earth system science context, provides valuable insights into causality.

3. Results

3.1 Climatology and long-term trends

The TPW seasonality encompasses the spatiotemporal oscillations and divergences manifesting disparate climatic determinants. The TPW during the thermally elevated summer months ranges from 29–29.8 kg m^{-3} when the atmospheric medium demonstrates an augmented capacity for moisture retention attributable to escalated evaporation rates. Nonetheless, alternate seasons, such as spring and autumn, evince a mesoscopic TPW range from 28.7–29.4 kg m^{-3}, with a gradual upward trend from March to May and a gradual downward trend from September to November (Fig. 1a). The winter season shows the lowest TPW ranging from 28.3–28.7 kg m^{-3} due to myriad factors. The wintertime engenders substantial temperature declines, leading to diminished evaporation rates. Consequently, the reduced evaporation translates into an absence of moisture available for atmospheric suspension as water vapor.

Furthermore, colder air has a diminished moisture-holding capacity relative to warmer air, impeding water vapor retention even in the presence of limited moisture. Additionally, winter typically ushers in drier air masses originating from continental or polar regions, culminating in diminished atmospheric moisture content. These factors yield a pervasive reduction in TPW during winter, rendering it the season characterized by the most meager water vapor levels. The long-term trend of TPW provides profound insight into the metamorphosing kinetics of atmospheric moisture content. Empirical investigations indicate a plausible trajectory of increasing TPW (0.037 kg per m^{-3} per year) over the temporal expanse, emblematic of climate change's sway on water vapor dispersion (Fig. 1b). This ascendant trajectory holds ramifications for meteorological paradigms, engendering heightened precipitation events and augmented atmospheric volatility.

Nevertheless, regional disparities exist, necessitating meticulous appraisal of localized TPW transformations to fathom comprehensive repercussions on hydrological oscillations, aridity circumstances, and hydraulic resource administration. The tropical zones often experience escalated magnitudes (ranging from 40–60 kg m^{-3}) of water vapor content during their designated wet seasons. In contrast, temperate regions may encounter zeniths in this regard during summertime (Fig. 1c). Profound comprehension of the seasonality of TPW bears paramount importance in forecasting meteorological patterns, evaluating drought conditions, and investigating the repercussions of climate change on water accessibility. Subtropical regions exhibit varying levels of TPW throughout the year. Generally, these regions experience moderate to high TPW values ranging from 20–30 kg m^{-3} due to their proximity to warm ocean currents. However, TPW can fluctuate due to seasonal variations, monsoon patterns, and the influence of nearby weather systems. The polar regions, encompassing the Arctic and Antarctic, reveal the most meager TPW levels ranging from 2–10 kg m^{-3} by a confluence of intrinsic determinants germane to their distinctive climatological circumstances.

Furthermore, the polar realms endure protracted, light-deprived winters bereft of solar irradiance. This shortage of solar radiation engenders constrained energy availability for evaporation mechanisms, thus further abetting the paucity of TPW. Moreover, expansive ice sheets and snow-covered surfaces typify the polar regions, which engender heightened albedo and attenuated thermal absorption and evaporation. The atmosphere's moisture reservoir contributing to TPW is notably curtailed with diminished evaporation.

The TPW trend in tropical (0.08–0.1 kg per m^{-3} per year) and subtropical regions (0.025–0.050 kg per m^{-3} per year) increased TPW levels in tropical and subtropical regions (Fig. 1d). However, the Indo-Pacific and Indian Ocean regions show the highest most increasing trend ranging from 0.09–0.10 kg per m^{-3} per year. This trend is attributed to several factors influenced by climate change. Warmer temperatures in these

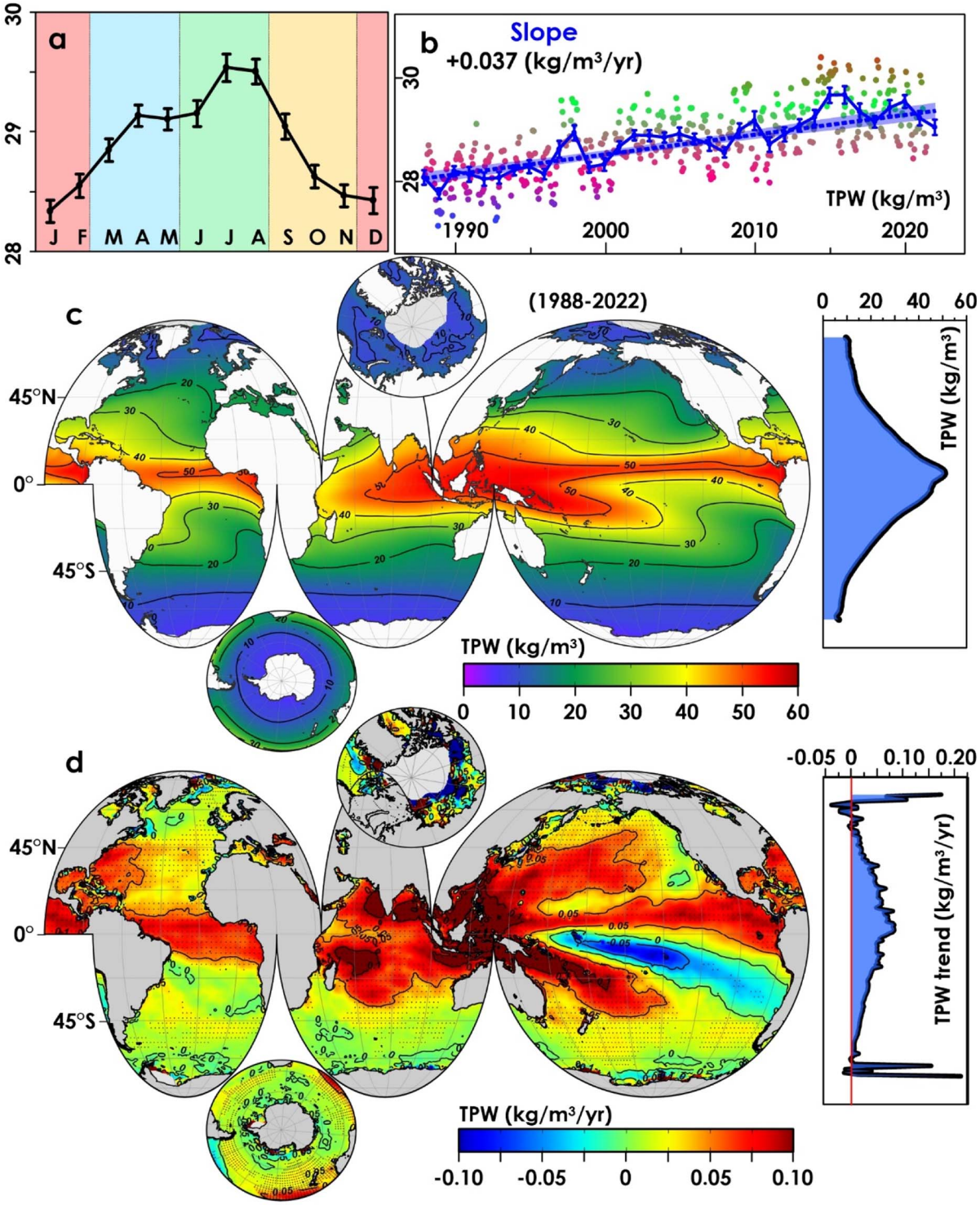

Fig. 1 The global long-term mean monthly and seasonal variation of total precipitable water (a), along with a time series depicting a linear trend line (b) and the spatial distribution of climatology (c) with a long-term linear trend overlaid with black dots representing significance at the 95% confidence interval (d).

regions promote enhanced evaporation rates, increasing atmospheric moisture availability. Increasing SST contributes to greater ocean evaporation, which subsequently elevates TPW levels. Additionally, changes in atmospheric circulation patterns, such as the intensification of monsoonal systems, can influence TPW in tropical regions. The Indo-Pacific region has been witnessing an increasing trend in TPW levels due to the ENSO shifts in monsoonal systems and the strengthening of tropical convergence zones. The polar regions have been experiencing notable changes over recent years. A positive trend

(0.01–0.02 kg per m^{-3} per year) in polar regions is melting ice sheets and glaciers. Ice releases water into the atmosphere as the ice melts, thereby increasing TPW levels. The loss of sea ice coverage also plays a role in TPW changes by enabling more moisture to be absorbed into the polar atmosphere.

3.2 Seasonal distribution and long-term seasonal trends

In the transition from winter to spring, the Northern Hemisphere experiences an increase in temperatures, which enhances ocean surface evaporation and increases atmospheric TPW levels ranging from 25–35 kg m^{-3} (Fig. 2). Subsequently, during summer, the NAO attains its warmest state, fostering heightened evaporation rates and, consequently, the highest levels of TPW ranging from 30–55 kg m^{-3}. As autumn ensues, temperatures cool, tempering evaporation but maintaining high TPW, ranging from 30–50 kg m^{-3} due to heat retention. During winter, the cooler ocean yields diminished evaporation and lower TPW levels ranging from 20–30 kg m^{-3}. NAO has a positive trend in autumn and summer, 0.05–0.08 kg per m^{-3} per year, and 0.02–0.06 kg per m^{-3} per year in spring and winter. In spring, the SAO experiences an increase in temperatures, fostering enhanced evaporation and elevated TPW levels of 20–

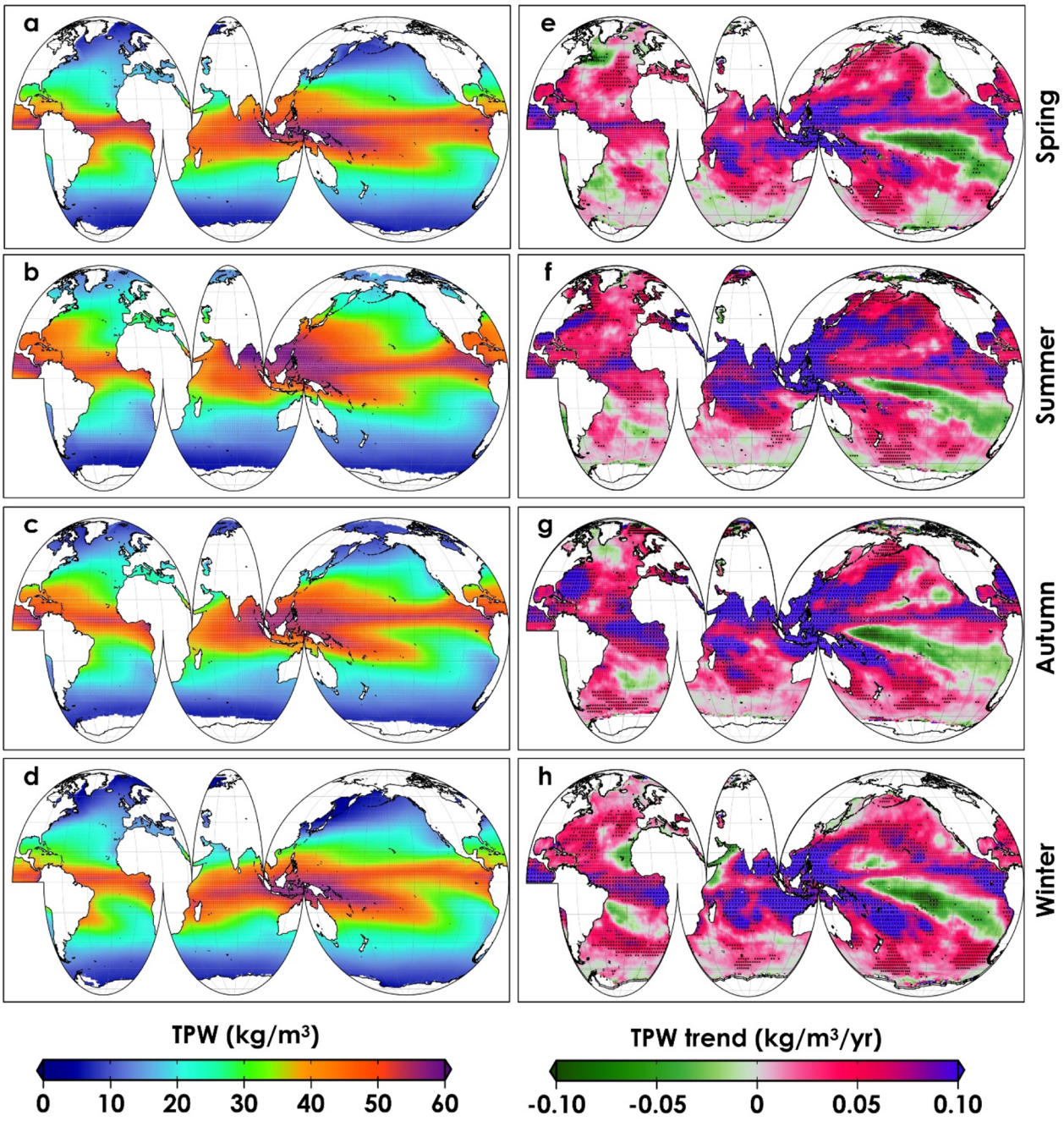

Fig. 2 The global long-term seasonal mean (a–d) and long-term seasonal linear trend with the significance at 95CI (e–h).

40 kg m^{-3}. In summer, correspondingly high values of TPW range from 22–36 kg m^{-3}, primarily in the equatorial region. Subsequent autumn months witness cooling temperatures, moderating evaporation, yet retaining residual heat, which sustains relatively high TPW levels ranging from 25–35 kg m^{-3}. During the southern hemisphere winter, the South Atlantic Ocean is more astonishing, contributing to reduced evaporation rates, lower atmospheric water vapor content, and diminished TPW values. NAO has a high positive trend in spring and summer, 0.03–0.05 kg per m^{-3} per year. Still, SAO shows a comparatively lower positive trend, and the central region also offers a negative trend ranging from −0.01 to −0.02 kg per m^{-3} per year. There is a similar trend pattern in autumn and winter, but values are slightly lower.

During spring, varying temperature patterns influence TPW in the Indian Ocean. In western and southern areas, where the TPW ranges from 40 to 55 kg m^{-3}, contrasting drier conditions are observed, while in the northern and eastern regions, TPW levels are lower, ranging from 20 to 30 kg m^{-3}. Regional factors, including the Indian summer monsoon onset, further influence TPW distribution. In summer, TPW is 45–55 kg m^{-3} in western and southern areas, contrasting drier conditions with lower TPW (35–45 kg m^{-3}) in the northern and eastern regions. Autumn exhibits diverse weather patterns, sustaining water vapor levels in some locales while witnessing decreased evaporation and water vapor content in others as they approach winter. The Indian Ocean experiences various climatic conditions during winter, with differential evaporation rates and atmospheric water vapor content in distinct regions. Equatorial and tropical areas maintain relatively stable temperatures with marginally higher TPW levels. In the Indian Ocean, all seasons show a positive trend ranging from 0.06–0.09 kg per m^{-3} per year, but in winter the western Indian Ocean offers a high negative trend of −0.08 to −0.08 kg per m^{-3} per year. The highest trend occurs in summer and autumn, ranging from 0.08–0.10 kg per m^{-3} per year.

In spring, temperatures amplify ocean surface temperature, augmenting atmospheric water vapor content. TPW levels increase incrementally during spring from 30–50 kg m^{-3}. Subsequently, summer unfolds as the warmest season in the North Pacific Ocean, with elevated temperatures driving intensified evaporation, resulting in significantly heightened TPW ranging from 35–60 kg m^{-3}. Conversely, autumn's cooling temperatures abate evaporation, yet residual ocean and atmospheric heat sustain a comparative increase in the TPW levels (30–50 kg m^{-3}). In the winter, the North Pacific Ocean exhibits cooler conditions, reducing evaporation rates and yielding relatively diminished atmospheric water vapor content, thus leading to lower TPW levels ranging from 20–42 kg m^{-3}. Temperature escalation fosters heightened evaporation in the spring in the South Pacific region, augmenting atmospheric water vapor content. A gradual increase in TPW ensues during the spring months, ranging from 30–56 kg m^{-3}. The subsequent summer is the warmest season, with elevated temperatures inducing significantly increased evaporation rates, yielding an increase in the TPW from 40–60 kg m^{-3}.

Conversely, autumn's cooling temperatures curb evaporation, while residual ocean and atmospheric heat sustain comparably elevated TPW. In the southern hemisphere winter, the South Pacific Ocean manifests more excellent conditions, diminishing evaporation rates and resulting in relatively lower atmospheric water vapor content, yielding decreased TPW values. The Pacific Ocean shows a high positive trend in all seasons, ranging from 0.04–0.06 kg per m^{-3} per year. However, the subtropical South Pacific Ocean (SPO) offers a very high negative trend ranging from −0.07 to −0.08 kg per m^{-3} per year in all seasons, and in spring, this accelerates to −0.008–0.010 kg per m^{-3} per year. Similarly, in summer, nearby California also shows a high negative trend ranging from −0.005–0.006 kg per m^{-3} per year.

As for the Arctic, spring temperatures increase, and ice begins to melt, increasing evaporation and boosting atmospheric water vapor levels. More significant open water areas and higher temperatures foster heightened evaporation rates and consequently higher TPW ranging from 10–20 kg m^{-3} in summer to 18–28 kg m^{-3}. Nevertheless, the Arctic's atmospheric moisture is typically lower than that at lower latitudes due to its colder and drier environment. During autumn, cooling temperatures reduce evaporation rates, causing potential decreases in TPW levels of 2–5 kg m^{-3}. In winter, the Arctic experiences frigid temperatures, limiting evaporation from the ice-covered ocean and generally resulting in lower TPW ranging from 5–15 kg m^{-3}. It is vital to acknowledge the Arctic's significant climate variability, which imparts variability in the seasonal distribution of TPW from year to year. All seasons show a shallow positive trend ranging from 0.01–0.02 kg per m^{-3} per year. However, the arctic cold blob region shows a negative trend in autumn, −0.02 to −0.03 kg per m^{-3} per year, and the highest in spring, −0.04 to −0.06 kg per m^{-3} per year.

In Antarctic autumn and winter, a gradual increase in temperatures initiates ice and snow melting, engendering increased evaporation and elevated atmospheric TPW ranging from 10–20 kg m^{-3}. IAntarctic spring summer, characterized by augmented sunlight and slightly higher temperatures, fosters more excellent evaporation rates; however, the overall atmospheric moisture content remains relatively low (5–12 kg m^{-3}) compared to other regions due to the continent's cold and dry environment. In all seasons, there is a very shallow positive trend ranging from 0.005–0.01 kg m^{-3} per year. However, spring shows a very shallow negative trend ranging from 0.01–0.02 kg per m^{-3} per year.

3.3 Key drivers

3.3.1 Sea surface temperature. The global SST climatology exhibits interoceanic variation: the Atlantic Ocean experiences an average SST spanning 15–30 °C, Pacific Ocean 18–32 °C, Indian Ocean 25–34 °C, Southern Ocean 5–12 °C, while that of the Arctic Ocean ranges approximately from 2.0 to 8 °C (Fig. 3a). The North Atlantic has demonstrated a positive climatic shift, characterized by a mean increment in SST of roughly 0.02 to 0.03 °C per year and within specific regions like Bermuda and nearby it is 0.035–0.040 °C per year (Fig. 3b). However, the south

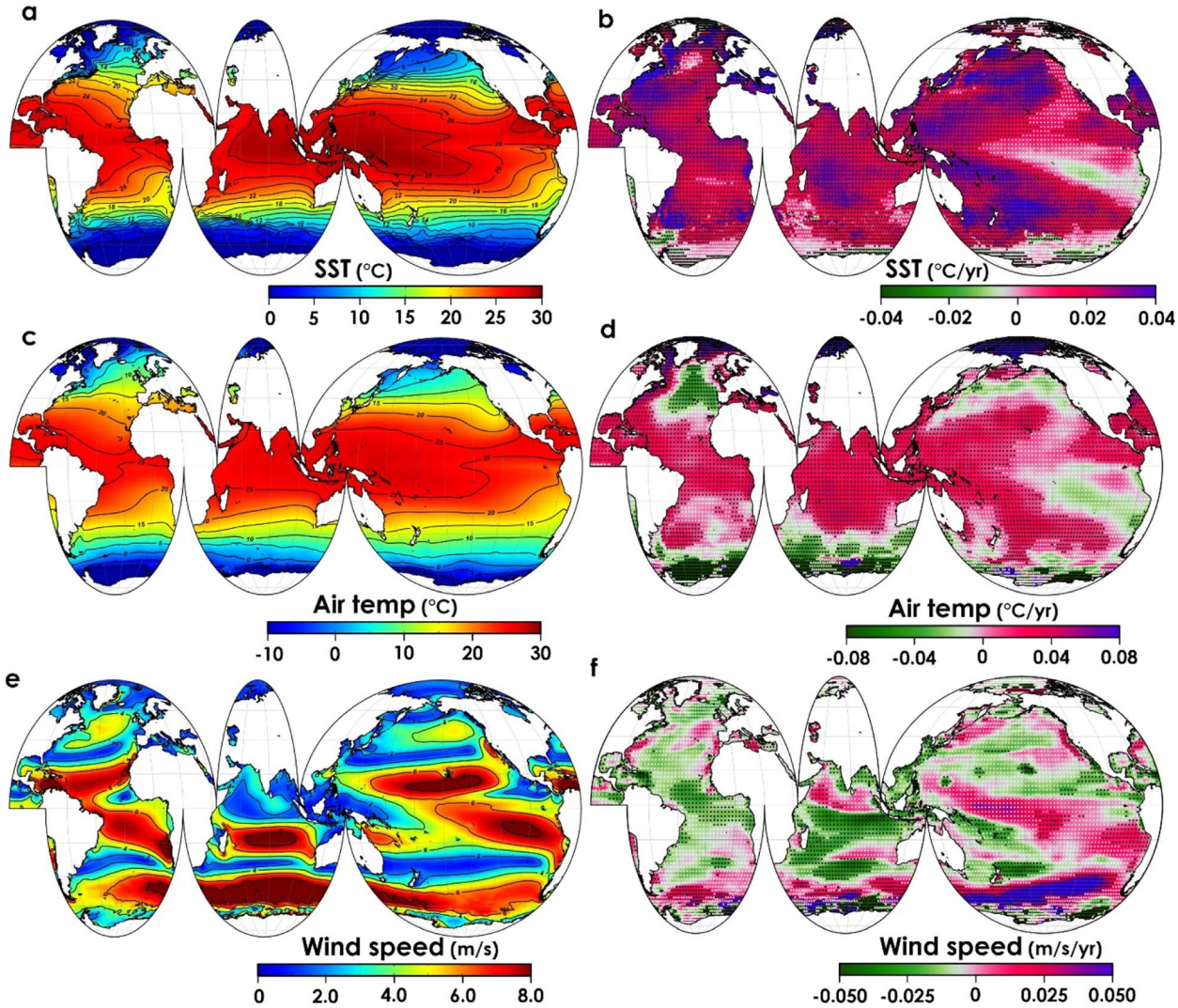

Fig. 3 The (a) climatology of sea surface temperature and (b) spatial trends (overlaid black dots represent the significance at 95CI). The others are the same as previous, but parameters are different, such as near-surface air temperature and wind speed (c–f).

Atlantic region shows a comparatively smaller warming trend 0.015 to 0.020 °C per year. The Equatorial Pacific has undergone dynamic oscillations linked to El Niño and La Niña phenomena, engendering heightened thermal amelioration or dissipation phases. Similarly, the northeastern Pacific, encompassing the California Current domain, has also exhibited a climatic inclination towards warming, approximating a trend of around 0.038 to 0.040 °C per year. The Indian Ocean, in its entirety, has manifested a discernible warming bias, with an average SST escalation of approximately 0.1 to 0.18 °C per year. In contrast, the warming tendency in the Southern Ocean displays heightened variability relative to other regions. Notably, the Antarctic Peninsula has encountered significant thermal augmentation, with rates ranging from approximately 0.020 to 0.025 °C per year, whereas other areas have manifested less pronounced warming or even cooling trends (−0.010 to −0.018 °C per year). The Arctic Ocean shows a negative SST trend (−0.005 to −0.010 °C per year). Still, the Beaufort, Chukchi, East Siberian, Laptev, and Barents Sea regions have experienced a warming trend, with rates averaging around >0.04 °C per year.

3.3.2 Near-surface air temperature. The near-surface climatology air temperature ranges exhibit substantial variation across diverse oceanic regions. Within the tropical Pacific, temperatures typically span 25 °C to 30 °C (Fig. 3c). The North Atlantic experiences a temperature range of 15 °C to 28 °C, with relatively warmer conditions in its southern sectors. The South Atlantic demonstrates a broader temperature spectrum, ranging from 10 °C to 26 °C, with colder zones in proximity to Antarctica and warmer zones nearer the equator. In the Indian Ocean, temperatures generally fall between 25 °C and 30 °C, with warmer conditions prevailing in its western expanses. The Southern Ocean shows lower temperatures, spanning approximately 2 °C to 8 °C, with colder regions closer to Antarctica. The Arctic Ocean registers roughly 4 °C to 12 °C, with low-temperature environments in its northern parts. These ranges are subject to variations attributed to seasonal fluctuations,

oceanic currents, and localized weather patterns. Different oceanic regions have exhibited varying near-surface warming trends. The tropical Pacific and North Atlantic have experienced a warming trend of approximately 0.03 to 0.04 °C per year, with higher rates observed in the subpolar regions of the North Atlantic (Fig. 3d). The South Atlantic demonstrates variable trends, with some areas experiencing a warming of around 0.02 to 0.03 °C per year. The Indian Ocean also shows a warming trend of about 0.04 to 0.06 °C per year but with regional variations. In the Southern Ocean, some regions, particularly closer to Antarctica, have seen a cooling trend of approximately −0.04 to 0.08 °C per year. The Arctic Ocean stands out with a pronounced warming trend of around 0.07 to 0.08 °C per year, with recent years experiencing accelerated warming. These trends reflect the dynamic nature of our oceans and their response to climate change.

3.3.3 Wind. In the tropical Pacific, wind speeds range from 7–7.5 m s^{-1}, with the prevalence of trade winds from the east to the west near the equator (Fig. 3e). However, during El Niño events, these trade winds weaken or reverse. The North Atlantic exhibits varying wind speeds ranging from 2–6 m s^{-1} due to the influence of prevailing westerlies and the North Atlantic oscillation (NAO). Additionally, wind speeds are impacted by storm systems, particularly in winter. In the South Atlantic, wind speeds range from 6–8 m s^{-1}, with stronger winds observed in the southern regions closer to Antarctica. Near the equator, trade winds are typically present. The Indian Ocean displays wind speeds ranging from 1–6 m s^{-1}, with the central south Indian Ocean experiencing higher rates of 7.5–8 m s^{-1}, influenced by the monsoon system, local weather patterns, and seasonal variations. Stronger winds were observed in the Arabian Sea and the Bay of Bengal during the southwest monsoon. The Southern Ocean, particularly at latitudes closer to Antarctica, is renowned for its strong winds exceeding 8 m s^{-1}. The polar vortex and the circumpolar westerlies drive these winds. The Arctic Ocean generally experiences wind speeds of 0.2–0.6 m s^{-1}, with stronger winds typically observed in autumn and winter. Wind patterns in the Arctic are influenced by sea ice extent and atmospheric conditions. The northern rim of the Southern Ocean exhibits a markedly high positive trend (>0.045 m s^{-1} per year). In comparison, a vast region in the South Pacific demonstrates a similarly notable positive trend ranging from 0.025 to 0.040 m s^{-1} per year (Fig. 3f). Conversely, the South Indian Ocean displays a prominent negative trend ranging from −0.025 to 0.035 m s^{-1} per year. However, other regions do not show significant increases or decreases in wind speed trends.

3.4 Causal discovery of global TPW with different climate indices

The intricate interaction between complex natural climate patterns and TPW is well established. Various climate phenomena strongly influence atmospheric phenomena and extreme events. The TWP receives positive feedback from PDO and ONI, with a cross-MCI value of 0.3 when α is 0.001 and a maximum time delay of 1 month (Fig. 4a). This relationship indicates that it can affect atmospheric circulation *via* changes in the position and strength of the jet streams, such as the Pacific and subtropical jets. Variations in the jet streams alter the transport of moisture across different regions, and impact TPW levels accordingly. Additionally, changes in atmospheric circulation associated with the PDO and ONI can influence the strength and frequency of weather systems like storms and fronts, further affecting TPW distribution and variability. WP has a direct and strong positive feedback loop (cross-MCI, 0.45) with TPW. This strong positive feedback can modulate the Asian monsoon circulation. Changes in SST and atmospheric pressure in the Western Pacific can alter the strength and position of the Asian monsoon, influencing moisture transport and precipitation patterns across the region. This, in turn, affects TPW levels by influencing the amount of moisture available in the atmosphere. However, PDO auto-MCI (0.002) is lower than that of ONI (0.35) at α level 0.1 (Fig. 4b), PDO and WP maintain the same relationship, but with a link with Western Hemisphere Warm Pool (WHWP) added at α level 0.5, a more robust and positive connection with TWP is observed (Fig. 4c). PDO's positive feedback strengthens, and TNA (tropical Northern Atlantic index), TSA (tropical Southern Atlantic index), and AAO (Antarctic oscillation) show a more prominent direct link (cross-MCI, 0.2). MEI (multivariate ENSO index) and DMI (dipole mode index) do not directly link with TPW but establish a clear link *via* WHWP (Western Hemisphere Warm Pool) within a 1 month time delay (τ_{max} 1 month).

In employing an α level of 0.001 and considering a 2-month time delay (τ_{max} 2 months), it is observed that PDO (Pacific decadal oscillation) and WP show a positive cross-MCI relationship with TPW. However, it is remarkable that the association between TPW and ONI (Oceanic Niño Index) is closely depicted (Fig. 4d). To delve further into these dynamics, an exploration is conducted by increasing the α level to 0.1. This high α level facilitated the identification of compelling associations with TWP. Specifically, WHWP, ONI, PDO, SOI (Southern oscillation index), DMI, and AAO (Antarctic oscillation) exhibited a notably strong relationship (cross-MCI, 0.2) with TWP (Fig. 4e). Among the various climate phenomena considered, it is notable that the only negative feedback observed was from TSA. In the context of an α level of 0.5, it is noteworthy that the previously established relationships persist unchanged (Fig. 4f). However, an intriguing observation is the emergence of a prominent indirect relationship between NAO (North Atlantic oscillation) and MEI through WP. An examination conducted at an α level of 0.001, with a 3-month time delay (τ_{max} 3 months), revealed that the previously established relationships involving PDO remained unchanged (Fig. 4g). Furthermore, at an α level of 0.1, the relationships with TPW exhibited minimal variation, except for the connection involving DMI which was disrupted (Fig. 4h). However, when the α level increased to 0.5, notable observations emerged. At this higher α level, it was observed that almost all climate indices displayed positive connections with TWP, except for TSA in a direct manner and AO (Antarctic oscillation) indirectly. At an α level of 0.001, the persistence of established connections implies their robustness and stability over time. However, the disrupted relationship with DMI at an

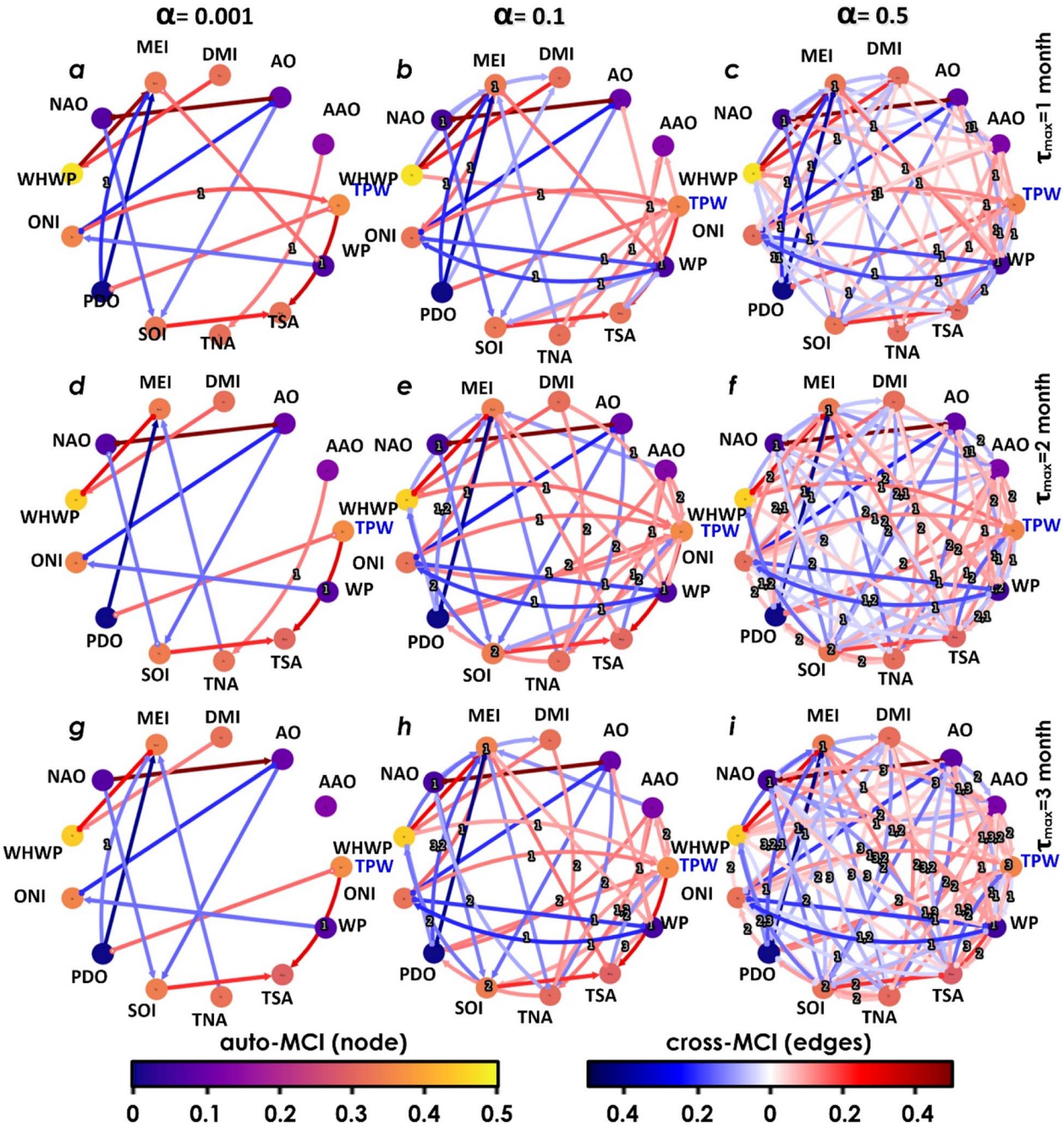

Fig. 4 First row shows the causal graphs representing the links for the relation of global TPW with the different climate indices. The maximum time delay denoted as τ_{max} is 1 month, alongside the significance threshold α, where α is varied at different levels: 0.01 (a), 0.1 (b), and 0.5 (c). In addition, the second and third rows show the same as the previous, but τ_{max} is 2 and 3 months (d–i).

α level of 0.1 suggests a potential sensitivity to variations in the α level. Of particular interest is the higher α level of 0.5, where a broader perspective reveals positive connections between TWP and most climate indices (Fig. 4i). This indicates a more decisive influence and interaction among these factors in driving variations in TWP. The direct connection between DMI and TWP reemerges at this level, further highlighting its significance in shaping TWP dynamics. However, it is essential to note that TSA exhibits a direct negative relationship with TWP, suggesting a potential inhibitory effect. Additionally, AO indirectly influences TWP, offering a more complex relationship through other intermediary factors.

3.5 Causal discovery of different oceanic region TPW with various climate indices

In the North Atlantic Ocean (NAO) region, there is vital positive feedback from TSA with a cross-MCI value of 0.5 at a constant α level of 0.1 and a maximum time delay of 1 month (Fig. 5a).

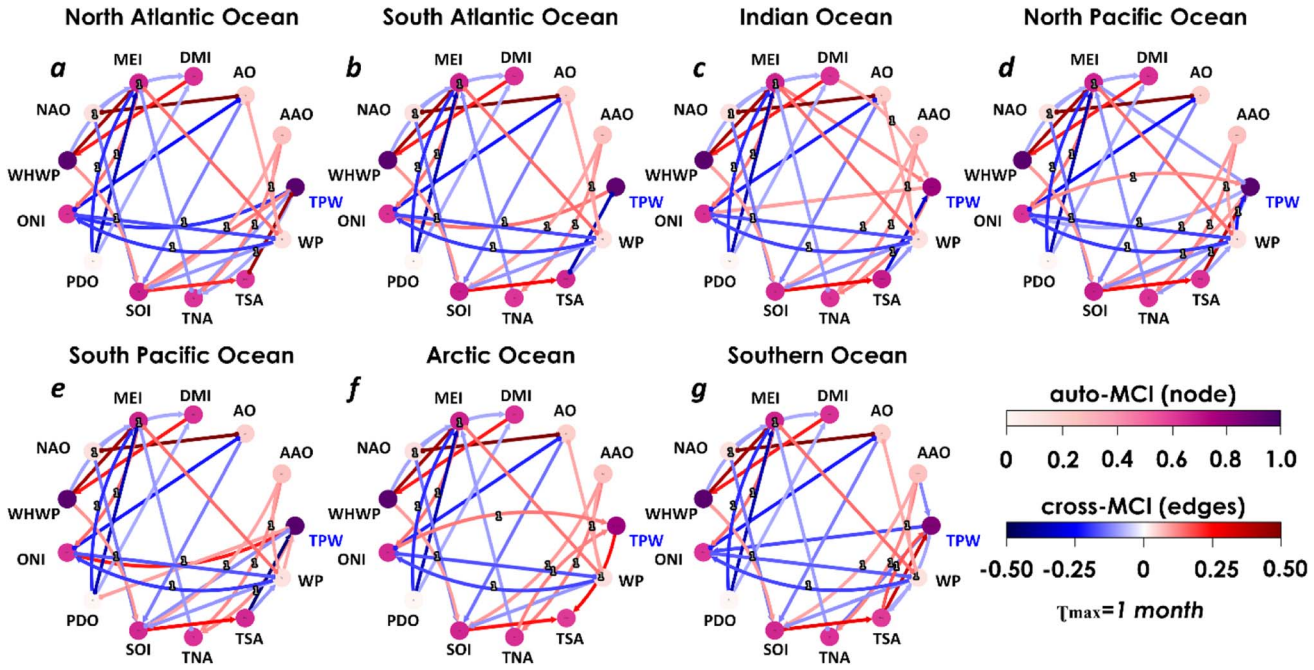

Fig. 5 Causal graphs of different natural climate patterns and TPW in different oceanic regions, the maximum time delay of one month ($\tau_{max} = 1$), and significance threshold $\alpha = 0.1$.

Conversely, the SOI also exhibits a positive connection, but with a lower cross-MCI value of 0.01. In the South Atlantic Ocean (SAO), positive cross-MCI is found with ONI. MEI demonstrates positive feedback through ONI (Fig. 5b). In the Indian Ocean (IO) region, DMI, MEI, ONI, and TNA provide positive feedback, with a cross-MCI of 0.25 (Fig. 5c). Conversely, in the North Pacific Ocean (NPO), ONI and SOI exhibit a positive connection with a cross-MCI of 0.1 (Fig. 5d). At the same time, TSA displays a robust positive connection with TPW with a cross-MCI value of 0.4. In the SPO, ONI shows a robust positive connection loop with a cross-MCI of 0.5, and PDO, WP, SOI, and TNA also show positive connections with TPW, with cross-MCI values ranging from 0.1 to 0.2 (Fig. 5e). In the AO, ONI and TNA exhibit positive feedback to TPW. WP shows a positive feedback loop with a cross-MCI of 0.4 (Fig. 5f). In the SO, TSA demonstrates a profound positive direct feedback to TPW with a cross-MCI of 0.5 and indirect feedback *via* other climate indices, where the cross-MCI is 0.3 (Fig. 5g).

Fig. S1† demonstrates that in the North Atlantic Ocean, at a maximum time delay of 2 months ($\tau_{max} = 2$), the Southern oscillation index (SOI) and tropical North Atlantic (TNA) exhibit a positive connection similarly at 3 months. However, the 3-month WP shows a positive feedback loop. Additionally, the North Atlantic oscillation (NAO) establishes a connection *via* the Arctic oscillation (AO) and WP, and the multivariate ENSO index (MEI) *via* WP. Meanwhile, the 4-month relationship remains consistent but with strengthened cross-MCI. In the South Atlantic Ocean, at a 2-month time delay, TNA and WP show a positive feedback loop, but at 3 months, the TNA connection is broken, and at 4 months, no teleconnection is evident. Fig. S2† reveals that at a 2-month time delay in the North Pacific Ocean, TPW shows a robust positive connection with Pacific decadal oscillation (PDO), ONI, tropical South Atlantic (TSA), and WP, with cross-MCI ranging from 0.2 to 0.3. The relationships remain primarily unchanged at 3 months and 4 months, but Arctic oscillation (AO) and MEI establish positive teleconnections *via* WP. In the South Pacific Ocean, at a 2-month time delay, ONI, PDO, and WP exhibit a robust positive feedback loop, and at 3 months, the relationships strengthen. At 4 months, TSA and SOI establish a new positive connection, while the ONI connection weakens. Fig. S3† shows that at a 2-month time delay, the multivariate ENSO index (MEI), dipole mode index (DMI), ONI, and TNA provide a profound direct positive feedback to Indian Ocean TPW. At 3 months, the MEI, DMI, and ONI connections close, but TNA and tropical South Atlantic (TSA) positive feedback is established. At 4 months, the TSA and TPW relationship strengthens, and WP shows a strong feedback loop. Fig. S4† reveals that in the minimum 2-month time delay, the Arctic Ocean indicates that ONI, TNA, and WP have a positive connection with TPW. At 3 months, the relationships remain mostly the same, but the WP connection is broken, and a TSA positive feedback loop is found. At 4 months, the TSA's positive feedback to TPW is closed. In the Southern Ocean, at 2 to 4-month time delays, TSA provides direct positive and indirect feedback *via* other climate indices. However, the TSA's direct positive connection weakens over time.

4. Discussion

Examining TPW's seasonality and long-term trends across diverse regions reveals distinct seasonal variations, with summer presenting elevated values due to heightened

evaporation rates. At the same time, winter exhibits lower values owing to reduced evaporation and drier air masses. Long-term trends signify an overall escalation in TPW, signifying the impact of climate change on water vapor dispersion. Regional disparities manifest, with tropical regions experiencing heightened TPW during wet seasons and temperate regions witnessing peaks in summer. A comprehensive comprehension of TPW's seasonality is imperative for meteorological predictions, drought assessment, and evaluating climate change's repercussions on water resources. Subtropical regions maintain moderate to high TPW levels year-round, influenced by warm ocean currents, seasonal fluctuations, monsoons, and nearby weather systems.

Conversely, polar regions exhibit minimal TPW levels due to restricted evaporation during light-deprived winters, extensive ice sheets, and snow-covered surfaces. The trend analysis uncovers ascending TPW levels in tropical and subtropical regions, with the Indo-Pacific and Indian Ocean regions displaying the most pronounced upward trend. Contributing factors encompass elevated temperatures, increased sea surface temperatures, alterations in atmospheric circulation patterns, and the influences of phenomena like ENSO and monsoonal systems. The polar regions also undergo notable transformations, with a positive trend linked to ice sheets and glacier melting, resulting in water release into the atmosphere and heightened TPW levels. Reducing sea ice coverage also enables augmented moisture absorption in the polar atmosphere.

Temperature variations and evaporation rates influence the observed seasonal trends in TPW in various ocean regions. In the spring, it leads to increasing temperatures, enhancing ocean surface evaporation, and increasing atmospheric TPW levels. Subsequently, during summer, the NAO experiences its warmest state, fostering heightened evaporation rates and resulting in the highest levels of TPW. As autumn ensues, cooling temperatures moderate evaporation but maintain high TPW levels due to heat retention. The more excellent ocean yields diminished evaporation in winter, leading to lower TPW levels, and similar temperature-driven trends are observed in the SAO, IO, and PO. The increase in temperatures during spring and summer leads to increased evaporation and higher TPW levels in these regions.

Conversely, cooling temperatures in autumn and winter lead to reduced evaporation and lower TPW levels. The Arctic experiences significant climate variability, leading to variations in TPW distribution. During spring and summer, increasing temperatures and melting ice contribute to increased evaporation and higher TPW levels. However, the Arctic's colder and drier environment keeps its atmospheric moisture content lower than that at lower latitudes. During autumn, cooling temperatures cause decreased evaporation and potential decreases in TPW levels. In winter, the Arctic experiences frigid temperatures, limiting evaporation and lowering TPW levels. In the Antarctic, a gradual increase in temperatures during autumn and winter leads to ice and snow melting, increasing evaporation, and elevated atmospheric TPW levels. However, the continent's cold and dry environment maintains relatively low overall atmospheric moisture content. Despite more excellent evaporation rates in spring and summer, TPW levels remain relatively low compared to other regions. These observed relationships between temperature patterns, evaporation rates, and TPW levels in different ocean regions are essential in understanding the Earth's water cycle and its influence on regional and global climate patterns. They play a crucial role in regulating the distribution of atmospheric water vapor and have implications for marine ecosystems, weather patterns, and global climate dynamics.

The North Atlantic demonstrates a positive climatic shift characterized by escalating sea surface temperature (SST) trends, while the South Atlantic exhibits comparatively subdued warming. The Equatorial Pacific and Northeastern Pacific exhibit discernible warming trends, in contrast to the Indian Ocean, which experiences a noticeable inclination towards warming. The Southern Ocean manifests enhanced variability, and the Arctic Ocean displays a negative SST trend, albeit with certain localized regions showing warming. Diverse areas exhibit varying near-surface warming trends, with the tropical Pacific, North Atlantic, Indian Ocean, and Arctic Ocean displaying warming tendencies. The South Atlantic demonstrates variable trends, and specific regions within the Southern Ocean show cooling trends. Wind speeds vary across oceanic regions, with trade winds prevailing in the tropical Pacific and near the equator. The North Atlantic experiences fluctuating wind speeds influenced by prevailing westerlies and storm systems. The South Atlantic, Indian Ocean, and Southern Ocean exhibit elevated wind speeds, with the Southern Ocean renowned for its robust winds driven by the polar vortex and circumpolar westerlies. The Arctic Ocean experiences relatively lower wind speeds impacted by the sea ice extent and atmospheric conditions. Certain regions display significant positive or negative trends in wind speed, notably the northern rim of the Southern Ocean and a vast area in the South Pacific.

Due to the complex nature of the interaction between natural climate patterns and TPW, at an α level of 0.001 and a 1 month time delay, positive feedback from PDO and ONI is observed, indicating their role in influencing TPW. The impact of PDO and ONI on TPW is often attributed to their influence on large-scale atmospheric circulation patterns. Changes in SST associated with PDO and ONI can affect atmospheric dynamics, leading to alterations in moisture transport and subsequent modifications in TPW levels. The WP (Western Pacific index) also exhibits a direct and strong positive feedback loop with TPW. The WP influences TPW through its effect on moisture transport and atmospheric dynamics. Positive WP phases are associated with enhanced convergence and upward air motion in the western Pacific, leading to increased moisture transport from the ocean surface into the atmosphere. This results in higher TPW levels. However, the strength of PDO's auto-MCI is lower than that of ONI at an α level of 0.1, suggesting potential variations in their impact on TPW. During the positive phase of PDO, which is associated with warmer SST in the northeastern and northwestern Pacific, TPW tends to increase. This positive relationship indicates that when PDO is in its positive phase, there is a higher likelihood of high TPW levels. Notably, at an α level of 0.5, a more robust and positive link with TWP is

observed, with PDO's positive feedback strengthening and TNA (tropical Northern Atlantic index), TSA (tropical Southern Atlantic index), and AAO (Antarctic oscillation) showing a more prominent direct link. MEI and DMI do not directly link with TPW but establish a clear connection *via* WP within a 1 month delay. The MEI does not exhibit a direct influence on TPW. However, it indirectly influences TPW by impacting large-scale atmospheric circulation patterns. El Niño events, associated with positive MEI values, can lead to changes in atmospheric circulation, affecting moisture transport and TPW levels. El Niño events are often linked to increased TPW.

On the other hand, the DMI represents the atmospheric variability between the Indian Ocean and the western Pacific. DMI influences TPW by modulating the region's atmospheric circulation patterns and moisture transport. On increasing the α level to 0.1, a stronger relationship with TWP was identified, involving WHWP, ONI, PDO, SOI, DMI, and AAO. Interestingly, TSA is the only index exhibiting negative feedback with TPW among the various climate phenomena considered. At an α level of 0.5, the previously established relationships persist unchanged, except for the emergence of a prominent indirect relationship between NAO and MEI through WP. The causal graph emphasizes the intricate interactions between climate patterns and TPW. They highlight the significance of considering different α levels and time delays to understand the complex dynamics.

The observed relationships between climate indices and TPW in various ocean regions provide valuable insights into the complex interactions that influence atmospheric moisture content. The significant positive feedback from TSA to TPW in the North Atlantic Ocean (NAO) region suggests that the warm and moist air masses from TSA contribute to higher TPW levels in the NAO. This feedback loop may intensify regional moisture availability and affect atmospheric circulation patterns. In the South Atlantic Ocean (SAO) region, positive cross-MCI with ONI indicates that El Niño events in the Pacific can influence TPW in the SAO, affecting moisture transport and regional climate. Furthermore, the positive feedback loop through MEI highlights the potential role of ENSO-related variability in regulating TPW in this region.

Similarly, in the Indian Ocean (IO) region, the positive feedback involving DMI, MEI, ONI, and TNA emphasizes the interconnected nature of different climate indices for influencing TPW levels. The relationships suggest that variations in these indices can lead to changes in atmospheric moisture patterns in the IO region. Conversely, in the NPO region, the positive connections of ONI and SOI with TPW indicate potential links between ENSO and the NPO moisture conditions. The robust positive feedback from TSA to TPW in the NPO suggests that TSA can be crucial in regulating atmospheric moisture content in this region. In the SPO region, the solid positive connection loop involving ONI and TPW implies that ENSO events substantially impact TPW variability in the SPO. The positive connections of PDO, WP, SOI, and TNA with TPW further highlight the influence of various climate indices on atmospheric moisture levels. In the Arctic Ocean (AO) region, the positive feedback loops involving ONI and TNA with TPW suggest that climate events associated with these indices can influence atmospheric moisture in the AO.

Additionally, the positive feedback loop with WP indicates the potential role of this index in modulating TPW in the AO. In the Southern Ocean (SO) region, the profound positive direct feedback from TSA to TPW highlights the significance of the South Atlantic's warm and moist air masses in regulating atmospheric moisture content in the SO. The indirect input *via* other climate indices underscores the complex interactions between different regions and their combined impact on TPW levels in the SO. Overall, the findings indicate that the interconnected nature of regional climatic processes, such as ENSO and other climate patterns, influences the relationships between climate indices and TPW. The positive feedback loops observed in various ocean regions emphasize the importance of understanding these interactions to comprehend and predict changes in atmospheric moisture content, which has crucial implications for regional and global climate patterns.

Hadley cell circulation plays a significant role in shaping global weather patterns and climate. In regions influenced by the Hadley cell, such as the North Atlantic Ocean (NAO) and South Atlantic Ocean (SAO), TPW levels may be influenced by the movement of warm, moisture-laden air masses associated with the Hadley cell. Positive feedback from climate indices like TSA and ONI in these regions may contribute to variations in moisture availability and TPW levels. Monsoon circulation affects precipitation patterns and moisture transport in regions like the Indian Ocean (IO) and SPO. TPW levels in these areas may vary seasonally in response to the seasonal wind reversals and shifts in the intertropical convergence zone (ITCZ) associated with monsoon systems. Positive feedback from climate indices like MEI and ONI may influence TPW dynamics through their impact on monsoon variability and moisture availability. Oceanic circulation patterns influence sea surface temperatures, moisture transport, and atmospheric circulation, which, in turn, impact TPW levels. Variations in ocean currents and gyres can affect regional climate variability and precipitation patterns, influencing TPW dynamics. Positive feedback from climate indices like DMI and TNA in the IO region may be linked to ocean–atmosphere interactions that influence TPW levels. Atmospheric teleconnections, such as those associated with the ENSO, can influence atmospheric circulation patterns and climate variability in distant regions. Positive feedback connections between climate indices like ONI, PDO, and TPW in the NPO and SPO regions may be influenced by teleconnection mechanisms that impact moisture transport and TPW levels.

The two-way causal link between TPW and the WP index is intricately woven through several atmospheric and oceanic processes. Firstly, ocean–atmosphere interactions, particularly during El Niño events, induce changes in atmospheric circulation, impacting moisture transport and thus TPW over the Western Pacific. Secondly, alterations in WPI-associated circulation patterns affect moisture convergence, influencing TPW levels. Thirdly, global atmospheric teleconnections like the Pacific-North American pattern modulate moisture transport, influencing TPW distribution. Furthermore, feedback

mechanisms between TPW and WPI-related circulation patterns reinforce this relationship. Lastly, interactions with regional climate features like monsoon systems further shape TPW–WP index dynamics, creating a complex interplay driving regional climate variability.

5. Conclusion

Analyzing the seasonal patterns and long-term trends of TPW across the World Ocean yields valuable insights into the intricate interactions shaping atmospheric moisture content. Seasonal variations in TPW are primarily driven by temperature, with higher TPW levels observed during warmer months due to increased evaporation rates. Conversely, cooler temperatures lead to reduced evaporation and lower TPW levels. Long-term trends reveal an overall increase in TPW levels, signifying the impact of climate change on water vapor dispersion. Regional disparities are evident, with tropical regions experiencing high TPW during wet seasons while temperate regions witness peaks in summer. Subtropical regions maintain moderate to high TPW levels year-round, due to seasonal fluctuations, monsoons, and nearby weather systems. The polar regions exhibit minimal TPW levels due to restricted evaporation during light-deprived winters, extensive ice sheets, and snow-covered surfaces. Understanding TPW's seasonality is crucial for meteorological predictions, drought assessment, and evaluating climate change's repercussions on water resources. The observed relationships between climate indices and TPW in different ocean regions reveal the interconnected nature of regional climatic processes, such as ENSO and other climate patterns. Positive feedback loops from various climate indices to TPW emphasize their role in regulating atmospheric moisture content. Changes in SST associated with these climate phenomena influence atmospheric dynamics, moisture transport, and TPW levels. The PCMCI+ algorithms have their limits in offering profound insights. To effectively address the complexities of air–sea interaction in our evolving climate, we require enhanced observation methods and intricately integrated, high-resolution Earth system models. These advanced tools hold the potential to unravel the intricacies of TPW dynamics and identify their underlying drivers with greater precision. Implementing policies to reduce greenhouse gas emissions and limit global warming is crucial in controlling TPW levels and their impact on regional climates. Efficient water management strategies are vital for meeting water demands in different regions. Collaborative efforts among countries and regions are essential to address transboundary water issues influenced by TPW variations.

Data availability

The TWP satellite microwave radiometer data can be accessed from the following publicly available source: **https://www.remss.com/**. Climate index data can be obtained from **https://psl.noaa.gov/data/climateindices/list/**. For MERRA-2 data, visit **https://gmao.gsfc.nasa.gov/reanalysis/MERRA-2/**. SST data are freely accessible at **https://climatedataguide.ucar.edu/climate-data/sst-data-noaa-high-resolution-025x025-(blended-analysis-daily-sst-and-ice-oisstv2)**.

Author contributions

SM: conceptualization, methodology, software, validation, formal analysis, investigation, resources, data curation, writing – original draft, writing – review and editing, visualization.

Conflicts of interest

The authors confirm no known conflicts of interest associated with this article.

Acknowledgements

I acknowledge the Indian Institute of Technology Kharagpur for facilitating the study. I also appreciate all the scientists who made available the data for this study.

References

1 T. M. Smith and P. A. Arkin, Improved historical analysis of oceanic total precipitable water, *J. Clim.*, 2015, **28**(8), 3099–3121.
2 N. S. Diffenbaugh, D. Singh, J. S. Mankin, D. E. Horton, D. L. Swain, D. Touma, *et al.*, Quantifying the influence of global warming on unprecedented extreme climate events, *Proc. Natl. Acad. Sci. U. S. A.*, 2017, **114**(19), 4881–4886.
3 J. Hansen, M. Sato and R. Ruedy, Perception of climate change, *Proc. Natl. Acad. Sci. U. S. A.*, 2012, **109**(37), E2415–E2423.
4 B. H. Tang, J. Fang, A. Bentley, G. Kilroy, M. Nakano, M.-S. Park, *et al.*, Recent advances in research on tropical cyclogenesis, *Trop. Cyclone Res. Rev.*, 2020, **9**(2), 87–105, DOI: **10.1016/j.tcrr.2020.04.004**.
5 J. H. Ruppert, A. A. Wing, X. Tang and E. L. Duran, The critical role of cloud–infrared radiation feedback in tropical cyclone development, *Proc. Natl. Acad. Sci. U. S. A.*, 2020, **117**(45), 27884–27892.
6 S. Gao, J. Mao, W. Zhang, F. Zhang and X. Shen, Atmospheric moisture shapes increasing tropical cyclone precipitation in southern China over the past four decades, *Environ. Res. Lett.*, 2021, **16**(3), 034004.
7 S. I. Seneviratne, N. Nicholls, D. Easterling, C. M. Goodess, S. Kanae and J. Kossin, *et al.*, Changes in climate extremes and their impacts on the natural physical environment. *Manag Risks Extrem Events Disasters to Adv Clim Chang Adapt Spec Rep Intergov Panel Clim Chang.*, 9781107025, 2012, pp. 109–230.
8 S. M. Hagos, L. R. Leung, O. A. Garuba, C. Demott, B. Harrop, J. Lu, *et al.*, The relationship between precipitation and precipitable water in CMIP6 simulations and implications for tropical climatology and change, *J. Clim.*, 2021, **34**(5), 1587–1600.

9 H. Douville, R. P. Allan, P. A. Arias, R. A. Betts, M. A. Caretta, A. Cherchi, *et al.*, Water remains a blind spot in climate change policies, *PLOS Water*, 2022, **1**(12), e0000058.
10 D. Ren, Y. Wang, G. Wang and L. Liu, Rising trends of global precipitable water vapor and its correlation with flood frequency, *Geodesy Geodyn.*, 2023, **14**(4), 355–367.
11 H. Ye, E. J. Fetzer, D. H. Bromwich, E. F. Fishbein, E. T. Olsen, S. L. Granger, *et al.*, Atmospheric total precipitable water from AIRS and ECMWF during Antarctic summer, *Geophys. Res. Lett.*, 2007, **34**(19), 1–5.
12 Y. Zhang, J. Xu, N. Yang and P. Lan, Variability and trends in global precipitable water vapor retrieved from COSMIC radio occultation and radiosonde observations, *Atmosphere*, 2018, **9**(5), 174.
13 S. Gao, S. Zhai, B. Chen and T. Li, Water budget and intensity change of tropical cyclones over the Western North Pacific, *Mon. Weather Rev.*, 2017, **145**(8), 3009–3023.
14 M. Liu, G. A. Vecchi, J. A. Smith and T. R. Knutson, Causes of large projected increases in hurricane precipitation rates with global warming, *npj Clim. Atmos. Sci.*, 2019, **2**(1), 1–5, DOI: **10.1038/s41612-019-0095-3**.
15 R. Chaluvadi, H. Varikoden, M. Mujumdar, S. T. Ingle and J. Kuttippurath, Changes in large-scale circulation over the Indo-Pacific region and its association with 2018 Kerala extreme rainfall event, *Atmos. Res.*, 2021, **263**(August), 105809, DOI: **10.1016/j.atmosres.2021.105809**.
16 M. R. Allen and W. J. Ingram, Constraints on future changes in climate and the hydrologic cycle, *Nature*, 2002, **419**(6903), 224–232.
17 N. Wunderling, F. Wolf, O. A. Tuinenburg and A. Staal, Network motifs shape distinct functioning of Earth's moisture recycling hubs, *Nat. Commun.*, 2022, **13**(1), 1–8.
18 R. Seager, N. Naik and G. A. Vecchi, Thermodynamic and dynamic mechanisms for large-scale changes in the hydrological cycle in response to global warming, *J. Clim.*, 2010, **23**(17), 4651–4668.
19 J. Lu, G. A. Vecchi and T. Reichler, Expansion of the Hadley cell under global warming, *Geophys. Res. Lett.*, 2007, **34**(6), 1–5.
20 M. Ting, Y. Kushnir, R. Seager and C. Li, Robust features of Atlantic multi-decadal variability and its climate impacts, *Geophys. Res. Lett.*, 2011, **38**(17), DOI: **10.1029/2011GL048712**.
21 S. Bony, B. Stevens, D. M. W. Frierson, C. Jakob, M. Kageyama, R. Pincus, *et al.*, Clouds, circulation and climate sensitivity, *Nat. Geosci.*, 2015, **8**(4), 261–268.
22 S. P. Xie, C. Deser, G. A. Vecchi, J. Ma, H. Teng and A. T. Wittenberg, Global warming pattern formation: Sea surface temperature and rainfall, *J. Clim.*, 2010, **23**(4), 966–986.
23 B. J. Soden and I. M. Held, An assessment of climate feedbacks in coupled ocean-atmosphere models, *J. Clim.*, 2006, **19**(14), 3354–3360.
24 R. A. Houze, Mesoscale convective systems, *Int. Geophys*, 2014, **104**, 237–286.
25 C. Schumacher and R. A. Houze, Stratiform rain in the tropics as seen by the TRMM precipitation radar, *J. Clim.*, 2003, **16**(11), 1739–1756.
26 J. Y. Lee, J. Marotzke, G. Bala, L. Cao, S. Corti and J. P. Dunne, *et al.*, IPCC. Climate change 2021: The physical science basis, *Future Global Climate: Scenario-42 Based Projections and Near-Term Information*, Cambridge University Press, Cambridge, UK, 2021, pp. 1–195.
27 A. Voldoire, D. Saint-Martin, S. Sénési, B. Decharme, A. Alias, M. Chevallier, *et al.*, Evaluation of CMIP6 DECK Experiments With CNRM-CM6-1, *J. Adv. Model. Earth Syst.*, 2019, **11**(7), 2177–2213, DOI: **10.1029/2019MS001683**.
28 F. J. Wentz and T. Meissner, Atmospheric absorption model for dry air and water vapor at microwave frequencies below 100 GHz derived from spaceborne radiometer observations, *Radio Sci.*, 2016, **51**(5), 381–391.
29 D. D. Turner, M. P. Cadeddu, U. Lohnert, S. Crewell and A. M. Vogelmann, Modifications to the Water Vapor Continuum in the Microwave Suggested by Ground-Based 150-GHz Observations, *IEEE Trans. Geosci. Remote Sens.*, 2009, **47**(10), 3326–3337.
30 J. Ding, P. Yang, M. D. King, S. Platnick, X. Liu, K. G. Meyer, *et al.*, A fast vector radiative transfer model for the atmosphere-ocean coupled system, *J. Quant. Spectrosc. Radiat. Transfer*, 2019, **239**, 1–44.
31 X. Jin, X. He, Y. Bai, D. Wang, J. Ying, Q. Zhu, *et al.*, A vector radiative transfer model for simulating the microwave emissivity of sea foam based on matrix operator method, *Front. Mar. Sci.*, 2023, **10**(May), 1–13.
32 C. A. Mears, D. K. Smith, L. Ricciardulli, J. Wang, H. Huelsing and F. J. Wentz, Construction and Uncertainty Estimation of a Satellite-Derived Total Precipitable Water Data Record Over the World's Oceans, *Earth Space Sci.*, 2018, **5**(5), 197–210, DOI: **10.1002/2018EA000363**.
33 C. A. Mears, J. Wang, D. Smith and F. J. Wentz, Intercomparison of total precipitable water measurements made by satellite-borne microwave radiometers and ground-based GPS instruments, *J. Geophys. Res.: Atmos.*, 2015, **120**(6), 2492–2504, DOI: **10.1002/2018EA000363**.
34 B. Huang, C. Liu, V. Banzon, E. Freeman, G. Graham, B. Hankins, *et al.*, Improvements of the Daily Optimum Interpolation Sea Surface Temperature (DOISST) Version 2.1, *J. Clim.*, 2021, **34**(8), 2923–2939.
35 R. Gelaro, W. McCarty, M. J. Suárez, R. Todling, A. Molod, L. Takacs, *et al.*, The modern-era retrospective analysis for research and applications, version 2 (MERRA-2), *J. Clim.*, 2017, **30**(14), 5419–5454.
36 J. Runge, P. Nowack, M. Kretschmer, S. Flaxman and D. Sejdinovic, Detecting and quantifying causal associations in large nonlinear time series datasets, *Sci. Adv.*, 2019, **5**(11), eaau4996.